

Local metal and deuterium ordering in the deuterated ZrTiNi C14 Laves phase

I. Levin^{*}, V. Krayzman, C. Chiu¹, K.-W. Moon, L.A. Bendersky

Material Measurement Laboratory, National Institute of Standards and Technology, Gaithersburg, MD 20899, USA

Received 24 May 2011; received in revised form 4 October 2011; accepted 12 October 2011

Available online 22 November 2011

Abstract

Local structure of the hexagonal C14 Laves phase in an annealed approximately equiatomic ZrTiNi alloy was studied before and after deuteration using neutron total scattering. Rietveld refinements of the $P6_3/mmc$ AB₂ model demonstrate that the A-sites are shared by Zr and Ti, whereas the two non-equivalent B-sites are occupied by a mixture of Ti and Ni. Reverse Monte Carlo refinements using a joint fit of the neutron total scattering data in real and reciprocal spaces revealed significant short-range ordering of Ti and Ni on the B-sites. The refined Ti–Ni nearest-neighbor distances are appreciably shorter than the corresponding Ti–Ti and Ni–Ni distances. Nevertheless, the differences in the effective sizes of chemically distinct tetrahedral interstices (i.e. [Zr₂Ti₂], [Zr₂TiNi], [Zr₂Ni₂], etc.), which are important for hydrogen absorption, remain rather small. Rietveld refinements of the structure of the deuterated sample TiZrNiD_{2.14} confirmed that deuterium occupies various [A₂B₂] tetrahedral interstices. RMC refinements suggested a strong preferential occupation of deuterium in the [Zr₂Ti₂] and [Zr₂TiNi] tetrahedra whereas the [Zr₂Ni₂] sites remained nearly empty. These results support earlier models which predicted preferential occupancy by hydrogen in sites coordinated by metals that form the most stable binary hydrides. The deuterium atoms in the [Zr₂TiNi] tetrahedra are displaced toward Ni. X-ray absorption near-edge structure measured for Ti, Zr, and Ni K-edges demonstrated that deuteration is accompanied by the reduction in the density of unoccupied electronic states (just above the Fermi level) associated with Ti and Zr.

Published by Elsevier Ltd. on behalf of Acta Materialia Inc.

Keywords: Hydrogen storage; Laves phases; Neutron diffraction

1. Introduction

Innovation in battery technology is required to realize vehicle electrification goals [1]. Nickel–metal hydride (NiMH) batteries, which store hydrogen in a solid hydride phase, are currently used in most hybrid vehicles and provide reliable and safe performance [2]. With the development of new electrodes, NiMH batteries may become competitive with the energy densities of lithium-ion batteries. Materials considered for advanced negative electrodes are based on multi-component Laves- or body-centered-cubic (bcc)-type crystal structures and store hydrogen

reversibly by filling interstitial tetrahedral sites [2]. Optimization of their performance is critically dependent on precise understanding of crystal chemistry and the energetics of populating these interstitial positions.

Laves phases AB₂ commonly crystallize with either cubic C15 (MgCu₂-type, space group $Fd\bar{3}m$) or hexagonal C14 (MgZn₂ type, $P6_3/mmc$) structures [3], which represent 3C and 2H polytypes, respectively, of tetrahedral closed-packed Frank–Kasper structures having a common slab composed of triangular and Kagomé layers. Laves phases absorb hydrogen in the tetrahedrally coordinated interstices; both structural types feature a total of 17 interstices per AB₂ formula [4,5]. The interstices are only partially populated and the number of absorbed hydrogen atoms rarely exceeds 5 (maximum 7) per AB₂ formula unit [5]. Both C15 and C14 (Fig. 1) binary Laves phases contain three chemically distinct types of tetrahedral sites available

^{*} Corresponding author.

E-mail address: igor.levin@nist.gov (I. Levin).

¹ Present address: Transportation Energy Technology, CanmetEnergy, Ottawa, ON, Canada K1A 1M1.

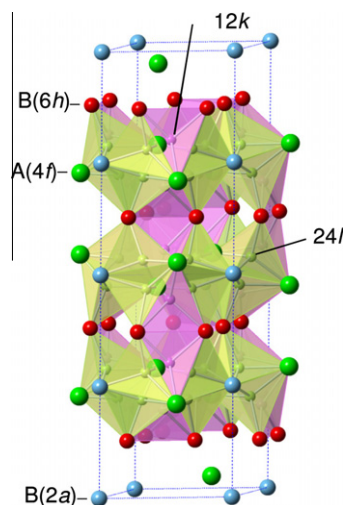


Fig. 1. A schematic drawing of the C14 structure. Metal A and B sites are indicated. The two $[A_2B_2]$ tetrahedral sites 24I and 12k that are preferentially occupied by hydrogen are indicated using polyhedra of different color. (For interpretation of the references to color in this figure legend, the reader is referred to the web version of this article.)

for hydrogen: $[B_4]$ ($\times 1$), $[AB_3]$ ($\times 4$), and $[A_2B_2]$ ($\times 12$). Most studies of hydrogenated Laves phases converge on the preference of hydrogen to occupy larger $[A_2B_2]$ sites followed by occupancy of $[AB_3]$ interstices, whereas the smallest $[B_4]$ tetrahedra typically remain empty [5]. The distances between the centers of face-sharing tetrahedra (<1.5 Å) are believed to be too short for hydrogen atoms to populate both neighboring sites; these restrictions constrain possible hydrogen distributions. Earlier theoretical calculations [6] suggested that H–H distances shorter than 2.1 Å are unfavorable because of H–H electrostatic repulsion (the so-called Switendick criterion). More recent experimental studies using nuclear magnetic resonance reported violations of this criterion in some hydrides, since H–H distances of ≈ 1.5 Å have been observed [7,8]; in Laves phases, these distances would correspond to H occupancy in nearest edge-sharing $[A_2B_2]$ interstices.

Commercial Laves-phase alloys designed for negative electrodes in NiMH batteries are typically multi-component systems with several species mixed on both A (Zr, Ti) and B (Ti, V, Cr, Mn, Ni) sites [2]. Rietveld refinements of the structures of several ternary Laves structures did not detect long-range order for the metal atoms, whereas analyses of deuterated samples confirmed a preference for D to occupy the $[A_2B_2]$ interstices [9]. However, average-structure refinements provide no information on the distribution of hydrogen over chemically distinct tetrahedra (e.g. $[A_2B'_2]$, $[A_2B''_2]$ or $[A_2B'B'']$ in the $A(B', B'')_2$ phase) or on the local distortions associated with hydrogen occupancy; yet, such detailed knowledge is critical for optimizing alloy compositions. Measurements of X-ray/neutron total scattering enable simultaneous determination of local and average atomic structures and therefore, in principle, can address this problem. Recently, applications of neutron total scattering to local-structure determination in several metal

hydrides have been reported [10–12], providing important, hitherto inaccessible, information on local hydrogen occupancies. Previous total scattering studies of hydrogenated Laves phases have been limited to C15-type $ZrCr_2D_4$, which features a single chemical type of $[A_2B_2]$ tetrahedra (i.e. $[Zr_2Cr_2]$) preferentially occupied by deuterium [12]. In the present study we combined determination of the average structure with analyses of a real-space pair-distribution function (PDF) obtained from the total neutron scattering to determine local structure in a Zr–Ti–Ni C14 Laves phase. This ternary system was selected because it yields approximately single-phase C14 samples near the equiatomic ZrTiNi composition, contains transition B-site metals (i.e. Ti and Ni) that exhibit different hydrogen affinities as well as dissimilar neutron scattering lengths ($b_{Ti} = -3.37$ fm, $b_{Ni} = 10.3$ fm), and displays appreciable hydrogen absorption at elevated temperatures/pressure with slow desorption at ambient conditions. This combination of characteristics was expected to facilitate detection of short-range metal and hydrogen ordering, if present.

2. Experimental

2.1. Sample preparation and initial characterization

An alloy ingot of nominal composition 38.7 Ti:33.3 Ni:28.0 Zr (at.%), hereafter referred to as ZrTiNi, was prepared by arc melting pure Ti, Zr and Ni on a water-cooled copper hearth under a high-purity argon atmosphere. The ingot was melted three times to ensure sample homogeneity. The as-cast alloy was vacuum-sealed in a quartz tube (7×10^{-6} Pa) filled with a helium gas. The sealed sample was annealed at 1073 K for 120 h. The overall composition of the annealed alloy was determined using inductively coupled plasma (ICP) measurements (Table 1). Imaging of the sample using back-scattered electrons in a scanning electron microscope (SEM) revealed the presence of primary (matrix) and secondary (inclusions) phases. Energy-dispersive X-ray spectroscopy (EDS) measurements, calibrated using the results of the ICP analyses, demonstrated that both phases exhibit similar elemental compositions (Table 1). EDS confirmed homogeneous distributions of constituent elements within the primary and secondary

Table 1

Results of compositional measurements (at.%) for the annealed ZrTiNi alloy. The EDS measurements were calibrated using the total composition determined from the ICP analyses. Numbers in parentheses refer to a single standard deviation in the measured concentrations. The concentrations and their standard deviations reported for the primary and secondary phases were obtained from the EDS measurements at 20 distinct locations within each phase.

Composition	Zr	Ti	Ni
Total (ICP)	27.9(1)	38.3(1)	33.7(1)
Total (EDS)	27.80(7)	38.33(7)	33.66(9)
Primary phase	27.79(6)	38.30(5)	33.91(7)
Secondary phase	26.6(2)	41.7(2)	31.76(5)

phases (e.g. measurements at 20 locations in the sample yielded a standard deviation of ≤ 0.1 at.%). Electron-backscatter diffraction (EBSD) patterns from the matrix matched the C14 structure while those from the secondary phase did not fit any of the Laves polytypes. The secondary phase identified in the present study is not included in the reported Zr–Ti–Ni phase diagrams.

X-ray diffraction (XRD) patterns were collected using a Panalytical X'Pert Pro² powder diffractometer equipped with a Ge incident beam monochromator ($\text{CuK}\alpha_1$ radiation) and a Pixcel position-sensitive detector. An XRD pattern from the as-cast sample (ground to a fine powder) exhibits relatively broad peaks, which can be readily indexed according to the C14 hexagonal structure, and a high background. The peaks sharpen considerably after the annealing but still exhibit abnormally broad bases. The background, albeit much lower compared to the as-cast sample, remains relatively strong and modulated. The C14 structure accounts for nearly all reflections apart from a few weak peaks (Fig. 2a) that were attributed to the secondary phase identified in SEM. Attempts to index these extra peaks using relevant known structures were unsuccessful. The concentration of Ni measured for the whole sample deviates significantly (95% confidence) from that in the primary phase, thereby enabling determination of the fraction of the secondary phase from the EDS data. A volume fraction of the secondary phase is estimated as ≈ 0.16 ; this relatively small fraction was ignored in subsequent structural analyses.

Measurements of hydrogen (deuterium) absorption were performed in a volumetric-type Sieverts apparatus. The system features a dosing volume of 47 cm^3 , a sample cell of 16 cm^3 , and two pressure transducers (0.1 MPa and 3.4 MPa) that span the pressure range up to 3.4 MPa. Gas uptake was measured by monitoring the pressure change in a closed volume. The sample was loaded in the stainless steel cell and heated in a tube furnace. The sample temperature was controlled to ± 1 K. Before each test, the system was leak-checked and then purged with a high-purity argon gas (99.999%) three times. System operation (opening and closing of valves) and data acquisition were controlled using in-house-developed Python software. The sample temperature and the pressure in the system were recorded every 5 s.

Deuterium is preferred over hydrogen for neutron powder diffraction because it exhibits a small incoherent scattering cross-section (≈ 2 barn for D vs. ~ 82 barn for H). Deuterated samples with the nominal deuterium concentrations of 1.06 wt.% were prepared by continuous absorption at 473 K under deuterium pressures of 0.5 MPa and 1.5 MPa, respectively. Samples were stabilized at 473 K under a dynamic vacuum (3×10^{-5} Pa) for 1 h before the deuterium gas (99.5%) was introduced. Once the deuterium

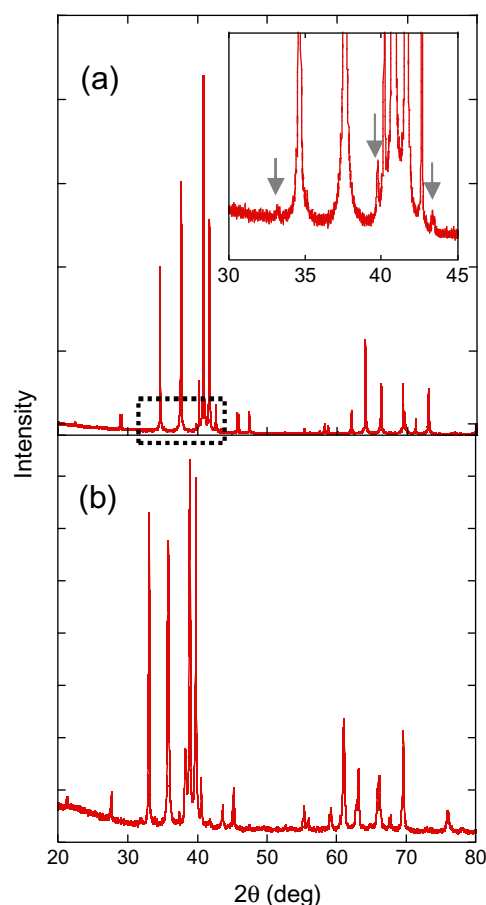


Fig. 2. X-ray diffraction patterns of (a) ZrTiNi (annealed) and (b) ZrTiNiD₂. In both cases, the reflections are accounted for by the C14 structure except for a few weak peaks attributed to an unknown impurity phase.

concentration reached its target value, the samples were cooled to room temperature. A deuterium concentration of 1.06 wt.% was reached after two runs at 0.5 MPa followed by one run at 1.5 MPa. This concentration of deuterium corresponds to 2.14 D atoms per metal–alloy formula unit; hereafter, the deuterated alloy will be referred to as ZrTiNiD₂.

The C14 structure was retained in the deuterated ZrTiNiD₂ sample (Fig. 2b). Deuteration caused expansion of the lattice volume from 195.73 Å^3 for ZrTiNi to 221.58 Å^3 for ZrTiNiD₂, and introduced considerable broadening of the Bragg reflections.

2.2. Neutron total scattering measurements and data reduction/analyses

Neutron total scattering data were collected at 300 K for the ZrTiNi and ZrTiNiD₂ samples using the NPDF instrument at the Lujan Neutron Scattering Center in Los Alamos. The samples were transferred to the neutron facility in sealed air-tight containers. The powders were loaded in vanadium containers in a glove box. Rietveld refinements were performed using the GSAS software package [13].

² The use of brand or trade names does not imply endorsement of the product by NIST.

The background shape was too complicated for an automated fit using common functions implemented in GSAS. Therefore, the backgrounds were fitted using a graphical option in EXPGUI [14]. The total scattering data were processed using the PDFGetN software [15] to extract the normalized scattering function $S(Q)$ and its corresponding real-space pair-distribution function $D(r)$ (hereafter, a notation after Ref. [16] is used):

$$D(r) = \frac{2}{\pi} \int_{Q_{\min}}^{Q_{\max}} Q[S(Q) - 1] \sin(Qr) dQ$$

A Q_{\max} value was selected at $\approx 30 \text{ \AA}^{-1}$.

Local structure refinements were performed using a reverse Monte Carlo (RMC) method [17] as implemented in RMCProfile [18]. This method employs large atomic ensembles and relies on a Monte Carlo algorithm to identify an atomic configuration that provides the best fit to experimental data. Unlike downhill algorithms used in Rietveld refinements, atomic moves that worsen the discrepancy between the calculated and experimental data are accepted with a probability that decreases exponentially as the misfit increases. An atomic move can be either an atom displacement or a swap of two atoms over their respective positions. Thus, the RMC method enables explicit treatment of both displacive and chemical disorder.

Despite considerable efforts to avoid exposure of deuterated samples to air, a limited deuterium–hydrogen exchange reaction took place as was manifested in the relatively high backgrounds caused by the strong incoherent neutron scattering from hydrogen. The incoherent scattering, which yields a broad maximum that differs drastically from the Q -dependence of the coherent background, was removed for each detector bank separately using the newly developed procedure outlined in Appendix A. Tests demonstrated that $D(r)$ was insensitive to the details of background subtraction for $r \leq 1 \text{ \AA}$; therefore, the minimum r value used in the refinements was set to 1.2 \AA .

Reverse Monte Carlo refinements were performed using an atomic configuration that included $12a \times 12a \times 7c$ hexagonal unit cells with a total of 12,096 metal atoms. The refinements involved a simultaneous fit of $G(r) = D(r)/4\pi r\rho(r)$, where $\rho(r)$ is the atomic number density. $G(r)$ was used because it emphasizes the local r -range better than $D(r)$. The Bragg profile was not included in the fit because of concerns that imperfect background descriptions in Rietveld analyses could bias the RMC refinements. For the non-hydrogenated sample, the starting configuration was based on the average atomic positions obtained from Rietveld refinements. Likewise, the fractions of species sharing the same crystallographic sites were fixed at the Rietveld-derived values. The RMC-refined configuration for ZrTiNi was used as the starting configuration for the metal framework in the deuterated structure. The deuterium occupancies of the distinct crystallographic sites were adopted from the Rietveld refinements and kept fixed during the RMC fits. The configuration for ZrTiNiD₂ contained a total of 22,438 atoms.

2.3. X-ray absorption fine structure measurements

X-ray absorption fine structure measurements were performed for the Ti, Ni, and Zr K-edges at the NIST X23A2 beamline at the National Synchrotron Light Source. For these measurements, the sample powders were dispersed on double-sided sticky tape. The measurements were performed at room temperature in transmission. An appropriate reference metal foil positioned downstream of the sample was recorded simultaneously with each scan for energy calibration. All data were processed using Athena software [20].

3. Results and discussion

3.1. Rietveld refinements

Rietveld refinements of the C14 (Fig. 1) hexagonal structure of ZrTiNi yielded a reasonable fit (Fig. 3) to the experimental neutron diffraction data, despite a complex background and broad bases of Bragg reflections. The refined structural variables included atomic coordinates, scattering powers at non-equivalent Wyckoff positions, and atomic displacement parameters (Table 2). The scattering power refined for each site was used to calculate atomic occupancies from the neutron scattering lengths. The A-sites (4f) were assumed to be occupied by a mixture of Zr and Ti atoms, whereas the B-sites (2a, 6h) were populated by a mixture of Ti and Ni. The refined structure (Table 2) is entirely consistent with that reported previously from neutron refinements of an as-cast Zr–Ti–Ni alloy with a C14 matrix of composition close to ZrTiNi [9]. The refined composition $\text{Zr}_{0.78}\text{Ti}_{1.002}\text{Ni}$ deviated slightly from $\text{Zr}_{0.82}\text{Ti}_{1.13}\text{Ni}$ determined by the ICP measurements. In

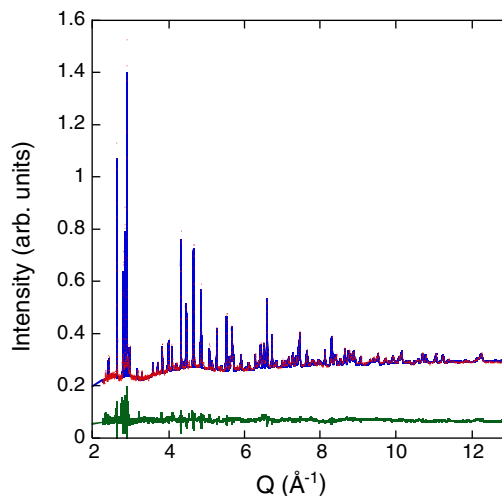


Fig. 3. Experimental (red) and calculated (blue, Rietveld) neutron powder diffraction patterns for TiZrNi. (148° bank, $R_{wp} = 2.11\%$). The total χ^2 value for the four banks (46°, 90°, 119°, and 148°) is 8.81. (For interpretation of the references to color in this figure legend, the reader is referred to the web version of this article.)

Table 2

Rietveld refinements of C14 in the annealed TiZrNi using neutron powder diffraction data. Space group $P6_3/mmc$, unit cell parameters $a = 5.17031(8)$ Å and $c = 8.45449(15)$ Å ($V = 195.727(5)$ Å³). Soft constraints were imposed on the total composition according to the ICP analysis (Table 1).

Atoms	Wyckoff position	x	y	z	Occupancy	$U_{\text{iso}} \times 100$ (Å ²)
Zr/Ti	4f	1/3	2/3	0.06757(9)	0.839(7)/0.161	1.32 ^a
Ti/Ni	2a	0	0	0	0.804(2)/0.268	1.3(3)
Ti/Ni	6h	0.83718(10)	0.67436(20)	1/4	0.390(5)/0.630	1.19 ^b

^a $U_{11} = U_{22} = 0.0123(3)$ Å², $U_{33} = 0.0148(5)$ Å², $U_{12} = 0.0062(2)$ Å².

^b $U_{11} = 0.0132(3)$ Å², $U_{22} = 0.0066(3)$ Å², $U_{33} = 0.0159(4)$ Å², $U_{12} = 0.0033(2)$ Å².

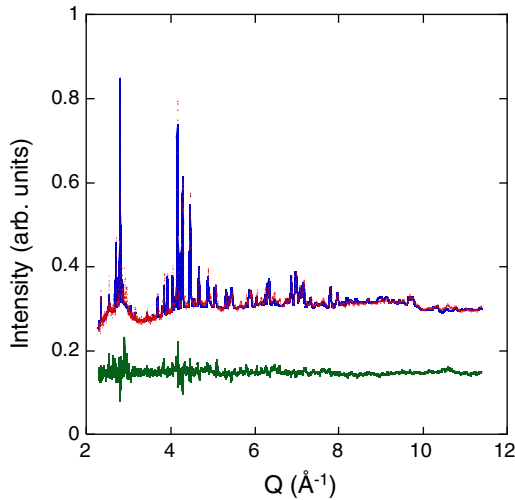


Fig. 4. Experimental (red) and calculated (blue, Rietveld) neutron powder diffraction patterns for TiZrNiD₂ (148° bank, $R_{\text{wp}} = 2.16\%$). The total χ^2 value for the four banks (46°, 90°, 119°, and 148°) is 8.99.

the final refinements, constraints based on the ICP results were imposed on the overall composition.

Rietveld refinement of the structure of ZrTiNiD₂ using the C14 model for metal atoms, and with deuterium atoms located in [A₂B₂] tetrahedral sites, generated a quality of fit comparable to that for the metal alloy prior to deuteration (Fig. 4). In these refinements, metal site occupancies were kept fixed according to the refined ZrTiNi structure. The refined parameters for the deuterated samples included atomic coordinates, displacement parameters, and site

occupancies for the tetrahedral interstices available within the metal framework (Table 3). The refined concentration of D (2.45 D per formula unit) is reasonably close to the nominal value (2.14 D) measured using the Sieverts apparatus. The refinements confirmed preferential D occupancy of the [A₂B₂] interstices. The most populated sites are 24f, 12k, and one of the 6h sites, which together accommodate 94% of the D atoms in TiZrNiD₂. The population of the [AB₃] sites (e.g. 4f) was negligibly small in TiZrNiD₂. The occupancies of the remaining tetrahedral sites (1 [AB₃] and 1 [B₄]) were also close to zero. Overall, the refined structure was consistent with the previous literature report [9] on the deuterated ZrTiNi Laves phase.

3.2. Reverse Monte Carlo refinements

3.2.1. ZrTiNi

The local structure of the ZrTiNi Laves phase was refined via simultaneous fitting of the $S(Q)$ and $G(r)$ data (Fig. 5). The Ti and Ni atoms were swapped during the refinements among the B-sites. This procedure reproducibly returned a certain degree of short-range Ti/Ni order; for example, the probability of finding a Ti atom in the first B-site coordination sphere of Ni was ≈ 0.57 compared to a random value of 0.48. The order was most pronounced on the 6h B-sites forming the Kagomé layers but detectable ordering correlations were also present between the 6h and 2b (triangular lattice) sites; a long-range order on both the Kagomé and triangular lattices is precluded by frustration effects. This short-range order of Ti and Ni increases a fraction of the [Zr₂NiTi] tetrahedra compared to a random

Table 3

Rietveld refinements of C14 in TiZrNiD₂ using neutron powder diffraction data. Space group $P6_3/mmc$, unit cell parameters $a = 5.38277(7)$ Å and $c = 8.83817(17)$ Å ($V = 221.771(7)$ Å³). Metal site occupancies were kept fixed at the values refined for the pristine alloy. No constraints were imposed on the D content. The volume change compared to the pristine alloy is 2.47 Å³ per D atom in the unit cell.

Atoms	Wyckoff position	x	y	z	Occupancy	$U_{\text{iso}} \times 100$ (Å ²)
Zr/Ti	4f	1/3	2/3	0.06757(9)	0.839(7)/0.161	2.64 ^a
Ti/Ni	2a	0	0	0	0.804(2)/0.268	1.0(5)
Ti/Ni	6h	0.83718(10)	0.67436(20)	1/4	0.390(5)/0.630	3.06 ^b
D	24f	0.0507(4)	0.3558(5)	0.5631(2)	0.265(2)	3.40(5) ^c
D	12k	0.4516(5)	0.9033(10)	0.6076(6)	0.158(2)	3.40(5)
D	6h	0.4410(9)	0.882(1)	1/4	0.130(3)	3.40(5)
D	6h	0.2113(5)	0.4227(9)	1/4	0.251(3)	3.40(5)

^a $U_{11} = U_{22} = 0.0247(5)$ Å², $U_{33} = 0.0293(11)$ Å², $U_{12} = 0.0124(3)$ Å².

^b $U_{11} = 0.093(6)$ Å², $U_{22} = 0.0035(4)$ Å², $U_{33} = 0.0491$ Å², $U_{12} = 0.0018(2)$ Å².

^c The U_{iso} parameters for all the D positions were constrained to be equal.

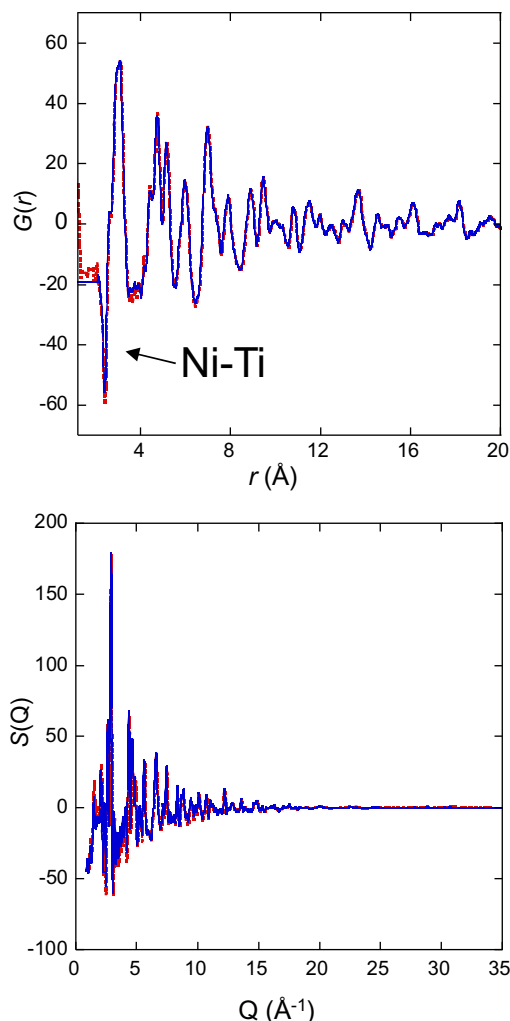


Fig. 5. Experimental (red) and fitted (blue, RMC) $G(r)$ and $S(Q)$ for ZrTiNi. (For interpretation of the references to color in this figure legend, the reader is referred to the web version of this article.)

metal distribution. Partial PDFs calculated for the refined configuration (Fig. 6) reveal that Ti–Ni distances are significantly (≈ 0.2 Å) shorter than both Ti–Ti and Ni–Ni distances; the latter two distances are similar to each other. Such shorter Ti–Ni distances combined with local ordering of Ti and Ni are consistent with the previous study [21], which suggested that in binary alloys having a tendency for ordering the distances between the dissimilar species are the shortest.

The size of a tetrahedral interstice can be characterized using the radii of the inscribed (R_{insc}) and circumscribed (R_{circ}) spheres for a given tetrahedron. For a perfect tetrahedron $R_{\text{circ}}/R_{\text{insc}} = 3$ and a deviation of this ratio from the ideal value reflects a distortion of the tetrahedron. Fig. 7 presents these radii and their ratio as calculated from the refined atomic coordinates for the distinct $[A_2B_2]$ tetrahedral sites occupied by D upon deuteration (i.e. $24k$, $12l$ and $6h$). The mean size of the $[Zr_2TiNi]$ tetrahedra is slightly smaller ($\Delta R \approx 0.01$ Å) than the sizes of the $[Zr_2Ni_2]$ and $[Zr_2Ti_2]$ tetrahedra; additionally, the $[Zr_2TiNi]$ tetrahedra are more distorted. These size differences appear to be

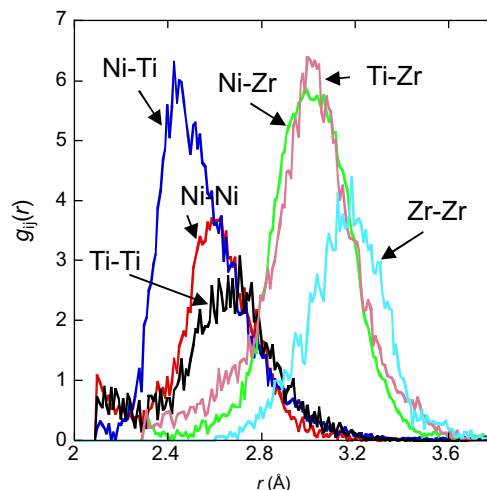


Fig. 6. Low- r parts of partial metal–metal PDFs for ZrTiNi.

too small to affect distribution of deuterium over various tetrahedral interstices.

3.2.2. $ZrTiNiD_2$

The atomic positions and site occupancies refined for the ZrTiNi alloy (Table 2) were used as a starting configuration for the metal atoms in $ZrTiNiD_2$ (the lattice parameters were set to those for $ZrTiNiD_2$). The D atoms were introduced randomly on each of the four types ($24k$, $12l$, $6h1$ and $6h2$, Table 3) of tetrahedral sites identified by Rietveld refinements with their concentrations fixed at the Rietveld-derived values. One configuration featured a random distribution of D, which was kept fixed during the fit. Another configuration allowed for a non-random D distribution, which was obtained by starting from the random distribution and then swapping D atoms over the four types of tetrahedral sites to obtain the best fit to the experimental data (during the swap, the concentration of D on each crystallographic site was kept fixed according to the Rietveld refinements).

A large total number of D sites rendered a simultaneous allowance for the swap and displacement moves impractical. Therefore, a two-step procedure was adopted. First, the D atoms were swapped over the tetrahedral sites to obtain the best fit to the data and then the positions of all the atoms in the configuration were relaxed to minimize the remaining discrepancies between the calculated and experimental data. RMC refinements of $ZrTiNiD_2$, a four-component system with species having both positive and negative neutron scattering lengths, are ill-constrained, so that several distinct configurations can provide similarly good fits to experimental data. Therefore, the chemical soundness of the refined structural characteristics must be considered rather than merely the quality of the data fit.

Refinements that involved swapping of D atoms over tetrahedral sites followed by relaxation of all atomic positions yielded a satisfactory fit (Fig. 8) to the experimental data and consistently generated a configuration with a strong

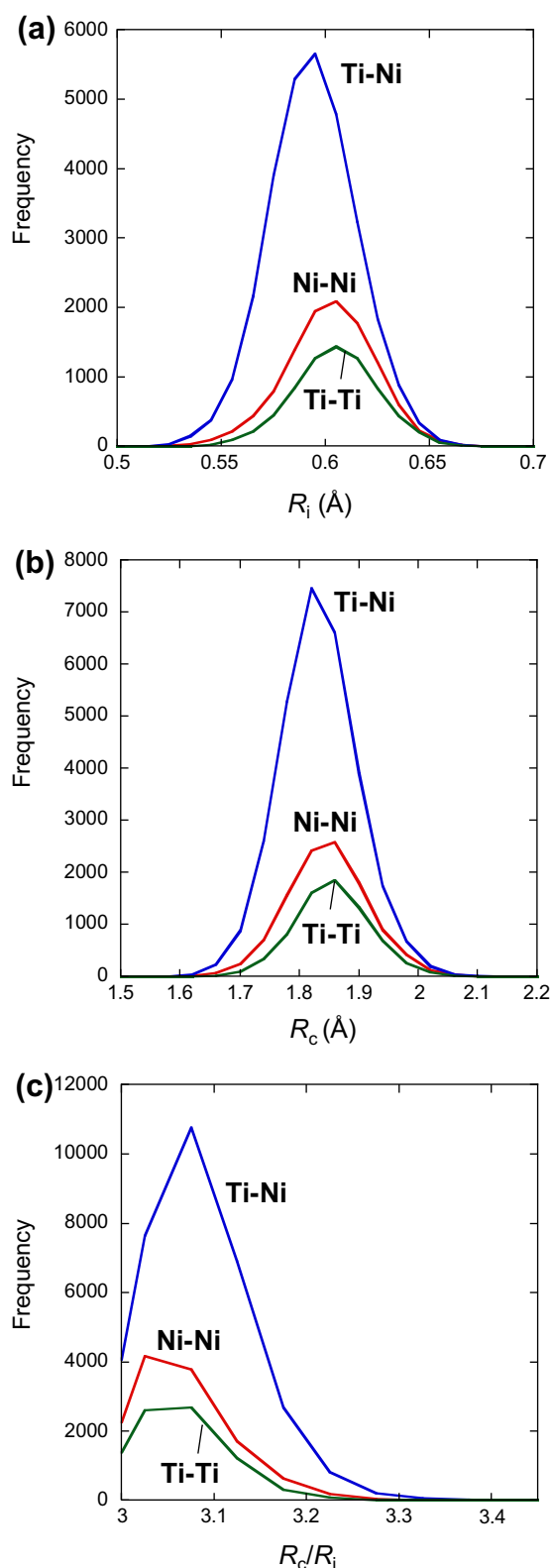


Fig. 7. Distributions of inscribed (a) and circumscribed (b) sphere radii and their ratio (c) for the chemically distinct $[A_2B_2]$ interstices that become occupied by D.

preferential occupation of D in $[Zr_2Ti_2]$ and $[ZrTiNi]$ sites, rather than $[Zr_2Ni_2]$ sites. However, the configuration with a random distribution of D and relaxed positions of all the

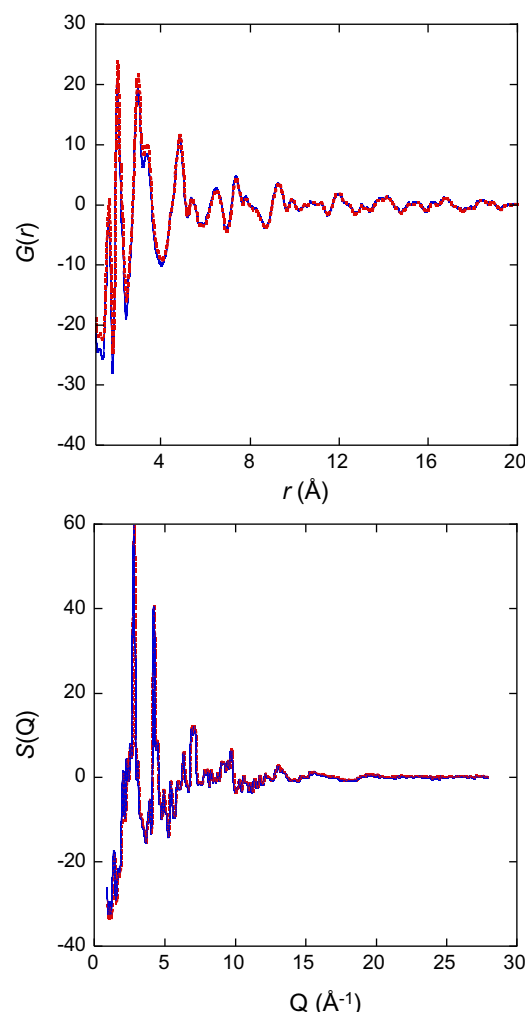


Fig. 8. Experimental (red) and fitted (blue, RMC) $G(r)$ and $S(Q)$ for $ZrTiNiD_2$. (For interpretation of the references to color in this figure legend, the reader is referred to the web version of this article.)

atoms produced a comparable quality of fit. The partial pair-distribution functions, $g_{ij}(r)$, calculated for the two refined configurations appeared to be qualitatively similar. In both cases, a double peak Ni–D distance distribution was obtained, whereas the Ti–D and Zr–D distributions featured a single peak (Fig. 9a). Analyses of the metal–D distances in individual tetrahedra revealed no systematic relation between the short and long Ni–D distances, suggesting that the double-peak Ni–D distribution is an artifact of the fit that arises due to a superposition of the partial PDFs having positive (i.e. Ni–D, Zr–D) and negative (Ti–D) contributions; in particular, the distances that correspond to the right peak ($r \approx 2.05$ Å) in the doublet appear to be unphysical (Fig. 9a). Indeed, Ni–H distances in all the reported metal hydride structures are shorter than 1.9 Å [22]. Since both random and non-random D configurations yielded PDFs with significant unrealistic features in the r -range that is most sensitive to the type of D distribution (i.e. random vs. non-random), a reliable selection of the correct distribution was impossible. Clearly, these two fits were under-constrained.

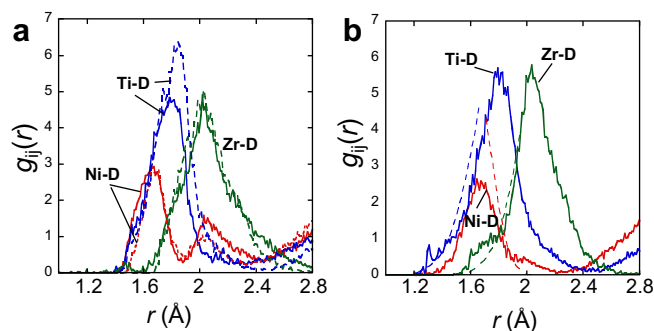


Fig. 9. (a) Low- r parts of partial metal–D PDFs obtained by unconstrained refinements for the non-random and random D distributions in chemically distinct $[A_2B_2]$ sites. Note a strong second Ni–D peak at larger r which is an artifact of the fitting. (b) The same partial metal–D PDFs obtained by constrained refinements for the D distribution having a strong preference for the Ti-based interstices. The unphysical Ni–D distances largely disappeared. The peak-tail restraints imposed on the partial metal–D PDFs are illustrated using dashed lines. Constrained fits using the configuration with a random D distribution (not shown) still produced large fractions of unphysical Ni–D distances.

The problem of unrealistically long Ni–D distances was addressed by introducing restraints on the first peaks in the metal–D partial PDFs. We developed soft polynomial-based restraints that constrained the problematic tail of the appropriate distance–distribution peak based on prior knowledge (from unconstrained refinements) of the remainder of the peak that appeared to be reliable (Appendix B). These restraints also incorporate the knowledge that partial PDFs are smooth, spike-free functions. The restraints control the accepted atomic moves via a penalty term introduced into the total residual function that restricts those atomic moves that cause $g_{ij}(r)$ to exceed the restraints function. The weights of these restraints in the total residual were reduced gradually during the fit and removed completely during the final stages of the refinements. Examples of such “peak-tail” restraints are illustrated in Fig. B1. These restraints are particularly effective in cases that involve an overlap of partial PDFs with positive and negative contributions.

The D swap under the peak-tail restraints imposed onto the Ni–D (high- r tail), Ti–D (low- r tail), and Zr–D (low- r tail) partial PDFs followed by relaxation of all the atomic positions produced a satisfactory fit to the data and a sound appearance of all the partial PDFs. Again, the swap suggested a strong occupational preference of D in the $[Zr_2Ti_2]$ and $[Zr_2TiNi]$ interstices (Table 4). Most of the Ni–D distances contribute to a single peak at distances somewhat shorter than those for the Ti–D distribution (Fig. 10), consistent with a smaller atomic radius of Ni compared to Ti. Despite significant efforts, even constrained refinements of the configuration with a random distribution of D returned large fractions of unphysically long Ni–D distances (2.1 Å). Clearly, a total number of the Ni–D distances in the random configuration is much greater than that present in the correct configuration. Thus, our results favor a non-random distribution of D with

Table 4

Fractions of chemically distinct 24f tetrahedra in several key structural models. Model 1: $ZrTiNi$ structure with a random distribution of Ti and Ni on the B-sites. Model 2: $ZrTiNi$ structure with short-range ordering of Ti and Ni as determined using RMC refinements. Model 3: Occupied by D in the $ZrTiNiD_2$ structure determined using RMC refinements.

Model	$[Zr_2Ti_2]$	$[Zr_2TiNi]$	$[Zr_2Ni_2]$	$[ZrTi_2Ni]$	Other ^a
1	0.19	0.39	0.12	0.15	0.15
2	0.17	0.45	0.08	0.18	0.12
3	0.37	0.33	0.004	0.17	0.126

^a $[ZrTiNi_2]$, $[Ti_4]$, $[Ti_3Ni]$, and $[Ti_2Ni_2]$ – the individual fractions of these tetrahedra that incorporate Ti on the A-sites are less than 0.05.

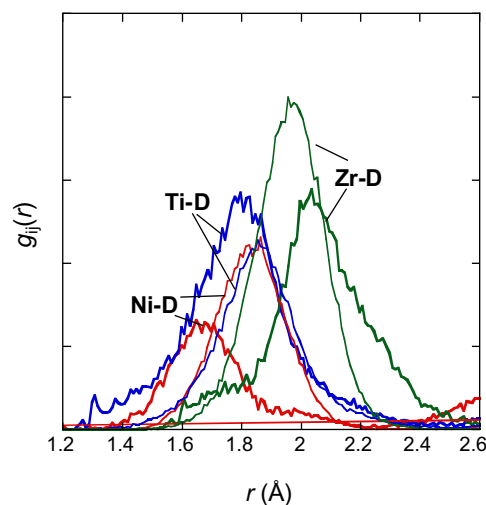


Fig. 10. Partial metal–D PDFs similar to those shown in Fig. 9b (thick lines) are compared to distributions of metal–“D” distances (thin lines) in the initial alloy (see text). Note shortening of Ni–D and Ti–D distances and expansion of Zr–D distances upon deuteration.

preferential occupancy of the $[Zr_2Ti_2]$ and $[Zr_2TiNi]$ sites because this configuration yields both a satisfactory fit to the experimental data and sensible structural characteristics.

Considering that the D swap and atomic-position relaxation were performed in sequence rather than simultaneously, the obtained D occupancies of chemically distinct tetrahedral sites should be treated as approximate. Furthermore, a small fraction of H substitution for D, resulting from the unintentional $D \leftrightarrow H$ exchange reaction during sample handling (see Section 2), which was neglected in the present refinements, inflates the apparent D occupancy of the Ti-based sites because of the negative neutron scattering length for H ($b_H = -3.74$ fm vs. $b_D = 6.67$ fm). However, additional refinements, where up to 20% of D atoms were replaced by H, showed that this relatively small H contribution cannot account for the very strong tendency of D to acquire the Ti-based coordination.

We further tested whether the presence/absence of the short D–D distances affects the conclusion regarding the D preference for Ti-based $[A_2B_2]$ interstices. In one case, a configuration was generated according to the Switendick criterion that requires $R_{D-D} > 2.1$ Å [6] without fitting the

experimental data. This configuration featured a nearly random (with regard to the metal coordination) distribution of D over chemically inequivalent $[A_2B_2]$ sites. Subsequently, all the atomic positions were relaxed until the best fit to the data was obtained. Alternatively, D atoms were first swapped under the Switendick criterion (i.e. $R_{D-D} > 2.1 \text{ \AA}$) to fit the experimental data and then all the atomic positions were relaxed to further improve the fit. The resulting D distribution consistently featured a strong preference for the Ti-based sites but now also conformed to the Switendick criterion. Refinements of the configuration with a random distribution of D over metal interstices again produced a good fit to the data but with unphysical partial metal–D PDFs. In contrast, a configuration with D preferentially occupying Ti-based sites, while yielding a good fit to the data, featured sensible partial PDFs: a minor number of unreasonable longer Ni–D distances could not be avoided but was considerably smaller compared to the “random” configuration. Thus, our inference about the D preference for the Ti-rich sites appears to hold regardless of the presence/absence of the short D–D distances.

Refinements under different constraints on the minimum D–D distances returned comparable fits and partial metal–D distance distribution functions. In the absence of well-defined data features determined by the short D–D distances, a reliable determination of the minimal D–D separation (relative to the Switendick criterion) proved impossible. A preference for the Ti-based D coordination (as opposed to the Ni-based) supports an earlier so-called imaginary binary hydride model, which predicts preferential H occupancy of the interstices formed by the metal atoms having the highest affinity for hydrogen [23].

Local-structure refinements can provide an insight into the local atomic relaxations upon deuteration. First, we used an atomic configuration refined for the non-deuterated ZrTiNi alloy to calculate the distances between the metal atoms and the interstitial sites (Rietveld-refined coordinates) that would become occupied by D; these are the distances ignoring volume expansion and atomic relaxations upon deuteration. Then, these distances were compared to the actual metal–D distances in $ZrTiNiD_{2.14}$ (Fig. 10). The Ni–“D” and Ti–“D” distance distributions in the non-deuterated alloy are similar and peaked at $\approx 1.86 \text{ \AA}$, whereas the longer Zr–“D” distances peaked at $\approx 1.97 \text{ \AA}$ (here “D” specifies ideal interstitial sites that are still empty in the alloy). The deuteration shortens Ni–D (peaked at $\approx 1.68 \text{ \AA}$) and Ti–D ($\approx 1.81 \text{ \AA}$) distances and elongates Zr–D distances ($\approx 2.09 \text{ \AA}$)³ compared to their unrelaxed values in the initial alloy. These results suggest that D atoms are strongly displaced toward Ni and Ti atoms away from Zr. The average Ni–D, Ti–D, and Zr–D distances agree reasonably well with the estimates based on sums of the relevant atomic radii. After deuteration, the difference

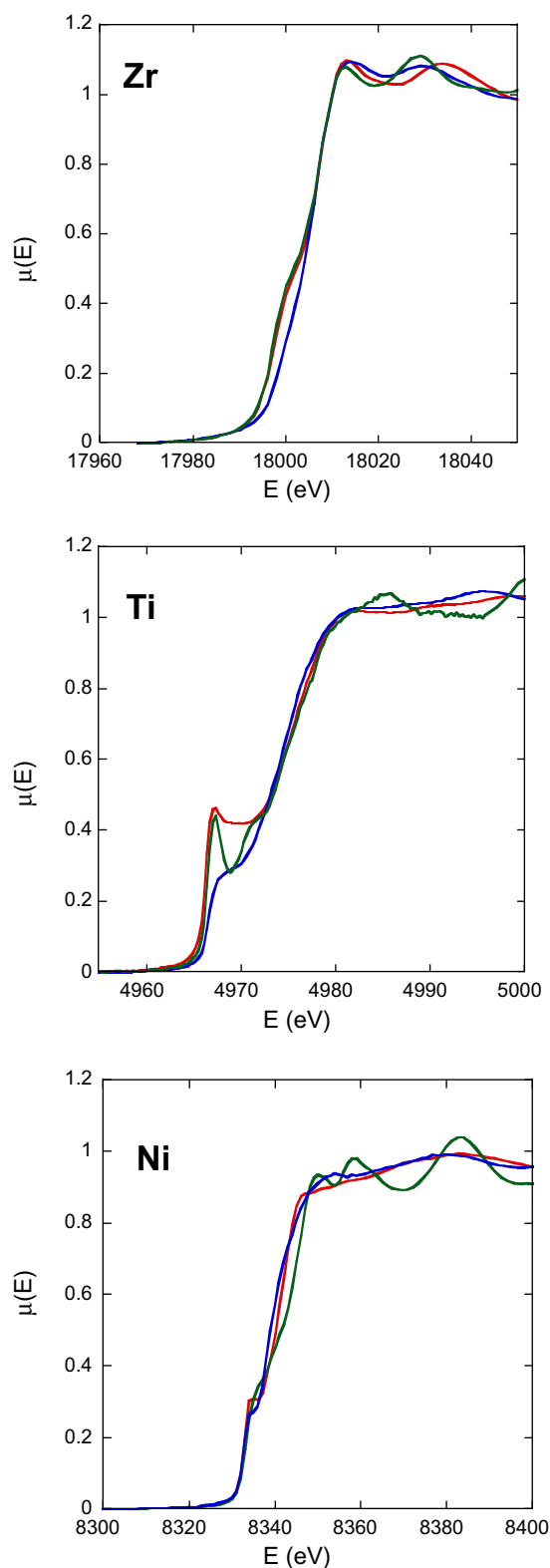


Fig. 11. X-ray absorption near-edge structure (XANES) for the Zr, Ti, and Ni K-edges in ZrTiNi (red), ZrTiD₂ (blue), and the corresponding reference metal foils (green). Note similarities between the spectra for individual metal components in ZrTiNi and pure metals. The density of unoccupied states (just above the Fermi level) associated with Ti and Zr decreases markedly upon deuteration. (For interpretation of the references to color in this figure legend, the reader is referred to the web version of this article.)

³ The shoulder at $\approx 1.7 \text{ \AA}$ in the Zr–D distribution (Fig. 9) is believed to be an artifact of the fit.

between the Ti–Ni and Ti–Ti/Ni–Ni distances seen in the pristine alloy becomes less pronounced and all the metal–metal distributions become considerably broader.

We also compared the distributions of inscribed and circumscribed radii for the occupied and empty tetrahedral interstices in ZrTiNiD₂. (In the starting configuration, all interstices were expanded uniformly compared to the initial alloy as determined by the imposed lattice parameters.) The refinements produced no significant differences between the radii for the filled and empty interstices. Possibly, fitting the pair-distribution functions that underlie the experimental data was insufficient to recover the details of higher-order correlations needed to describe distortions of the local tetrahedral coordination around D. However, the actual differences between the sizes of filled and empty interstices can be relatively subtle considering geometric constraints imposed by the connectivity of the filled tetrahedra. Theoretical calculations revealing local structure in hydrogenated Laves phases could help to clarify these issues but unfortunately none of the relevant theoretical studies reported so far has discussed the local distortions.

XANES spectra for Zr, Ti, and Ni in the ZrTiNi alloy (Fig. 11) are similar to those measured for the corresponding elemental metal foils, suggesting that the character of unoccupied states for individual metals is retained in the alloy. Deuteration leads to a significant reduction in the density of unoccupied states for Zr and Ti whereas no significant changes are observed for Ni. These changes are very similar to the results reported previously for simple metal hydrides ZrH_{1.98} and TiH_{1.90} [24], which suggests similarities between the effects of hydrogenation on the electronic structure of the ZrTiNi Laves phase and individual pure metals. Existing theoretical calculations on related Laves phases indicate that electron transfer from the metals to hydrogen atoms accompanies hydrogenation [25]. Concurrently, the energies of the metal *d*-bands are lowered with a decrease in the density of unoccupied states above the Fermi level [25]. Our XANES data are consistent with these theoretical predictions.

4. Conclusions

Rietveld refinements using neutron powder diffraction confirmed that the A- and B-sites in the nearly equiatomic ZrTiNi C14 Laves phase are occupied by Zr/Ti and Ti/Ni mixtures respectively. RMC refinements of this structure using neutron total scattering data revealed a clear tendency for short-range Ti/Ni ordering on the B-sites. The Ti–Ni distances are appreciably shorter compared to Ti–Ti and Ni–Ni. Consistent with previous reports, deuteration proceeds predominantly by D occupancy of the [A₂B₂] tetrahedral interstices. Deuterium preferentially fills the [Zr₂Ti₂] and [Zr₂TiNi] interstices while the occupancy of the [Zr₂Ni₂] sites remains relatively small. Such preference for D occupancy concurs with earlier models, which suggest that hydrogen favors sites coordinated by the metals that form the most stable hydrides. This short-range order of

D may still conform to the Switendick criterion because the present data provided no definitive evidence for D–D distances <2 Å. Maximizing the degree of short-range metal order (e.g. via selection of the appropriate annealing conditions) could increase considerably a fraction of Ti-coordinated interstices that are favored by hydrogen, thus possibly affecting hydrogen absorption. In the deuterated alloy, the D atoms are preferentially displaced toward Ni and Ti and away from Zr to form short and long Ni–D/Ti–D and Zr–D distances, respectively; the Ni–D distances are appreciably shorter than Ti–D. The refined metal–D distances agree well with estimates using sums of the respective atomic radii.

Acknowledgements

This work has benefited from the use of the Lujan Center at Los Alamos Neutron Science Center, funded by the Department of Energy Office of Basic Energy Sciences, and Los Alamos National Laboratory, funded by the Department of Energy under Contract W-7405-ENG-36. The authors are grateful to Joan Siewenie (LANL) and Joseph Woicik (NIST) for their technical assistance with the neutron and X-ray absorption measurements, respectively. X-ray energy-dispersive spectroscopy and electron backscatter diffraction measurements were performed by Alexander Berner (Technion – Israel Institute of Technology). Benjamin Chao and his colleagues at Ovonic Hydrogen Systems, LLC are acknowledged for their help with sample deuteration and ICP analyses.

Appendix A. A procedure for removal of incoherent scattering from $S(Q)$

The incoherent scattering that yields a broad maximum in Q -space is removed for each detector bank separately using the following procedure. First, RMCPProfile software is used to calculate $S(Q)$ for an atomic configuration based on the average atomic positions and displacement parameters obtained from Rietveld refinements. These simulations provide a sound baseline for the $S(Q)$ (Fig. A1a). Subsequently, a difference between the simulated and experimental $S(Q)$ is obtained, as shown in Fig. A1b. Note that the experimental $S(Q)$ is convoluted with a configuration box used in RMCPProfile. The baseline for this difference, which is largely due to incoherent scattering, is fitted by an empirical six-parameter analytical function:

$$f(Q) = P_1 e^{-P_2 Q} Q^{P_3} + P_4 / [(Q - P_5)^2 + P_6^2]$$

where P_i are the adjustable parameters. The analytical expression was selected over a polynomial or a B-spline (also tried) because it does not introduce any oscillations of the kind that may arise due to real structural correlations. Finally, this fitted baseline function was subtracted from the experimental data for each bank and the banks were merged (Fig. A1c). The baseline in the corrected data is close to that expected from coherent scattering; in fact,

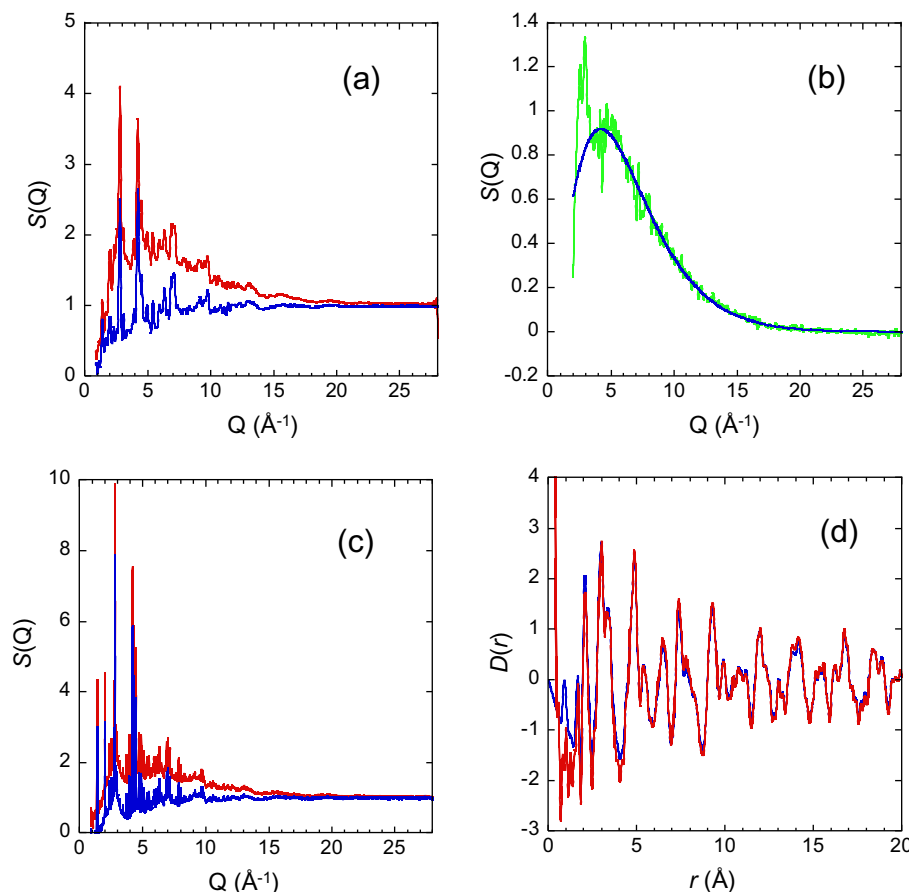


Fig. A1. A step-by-step illustration of the procedure for subtraction of incoherent scattering background from the neutron total scattering data. (a) Experimental $S_{\text{exp}}(Q)$ (red) and calculated $S_{\text{calc}}(Q)$ (blue) for ZrTiNiD₂. The calculated $S(Q)$ corresponds to a configuration based on the average atomic positions and atomic displacement parameters determined from Rietveld refinements. The experimental $S_{\text{exp}}(Q)$ was convoluted with the configuration box used in RMCProfile. (b) The difference $[S_{\text{exp}}(Q) - S_{\text{calc}}(Q)]$ for one the banks (119°) fitted using an analytical function $f(Q)$ described in the text. (c) $S_{\text{exp}}(Q)$ before (red) and after (blue) subtraction of $f(Q)$. (d) $D(r)$ obtained from the $S_{\text{exp}}(Q)$ before (red) and after (blue) background subtraction. Note the difference in the low- r range. (For interpretation of the references to color in this figure legend, the reader is referred to the web version of this article.)

the procedure described here not only corrects for incoherent scattering but also compensates for deficiencies in other additive corrections (e.g. inelastic scattering). The $D(r)$ obtained from the uncorrected and corrected data are compared in Fig. 4d. Note that incoherent scattering affected PDF (Fig. A1d) only for distances shorter than 2 \AA .

We tested the robustness of the above background-subtraction procedure for the case of deuterated ZrTiNi by using two configurations with random and non-random distributions of D over tetrahedral interstices, respectively, to simulate the baselines for the $S(Q)$; the configurations differed by the presence (random) or absence (non-random) of D–D distances shorter than <2 \AA . The $S(Q)$ generated for these two configurations were subtracted from the experimental data and the correction procedure was applied. The corrected pair-distribution functions were very similar to each other apart from the r -range below 1 \AA ; that is, a peak at ≈ 0.9 \AA in Fig. A1d, which in principle corresponds to the shortest H–H separation in the C14 structure, was dependent on the background subtraction procedure and as such was concluded to be unreliable.

Therefore, the r_{min} value used in the structure refinements was set at 1.2 \AA .

Appendix B. Peak-tail restraints in RMCProfile

Hard constraints on values of interatomic distances (i.e. minimum distances or distance windows) frequently lead to unphysical spikes/discontinuities in partial PDFs at the limiting distance values. This effect is most pronounced in systems with two closely overlapped partial PDFs having opposite signs of the Faber–Ziman coefficients because the artificial spikes in the two functions completely compensate each other in the total PDF. The problem can be alleviated by imposing restraints on peak tails in partial PDFs that enforce smooth and monotonic changes in the vicinity of the minimum and/or maximum interatomic distances for a relevant partial peak. The behavior of the peak tails is inferred from preliminary fits and must be justified by the prior knowledge of the system. For a given partial PDF $g_{ij}(r_j)$ and distance interval $[r_{\text{min}}, r_{\text{max}}]$, the restraints penalize those atomic moves which violate inequality

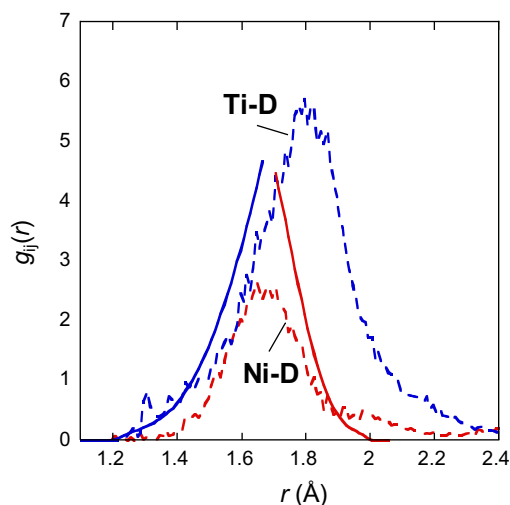


Fig. B1. Example of the peak-tail restraints (solid lines) imposed on Ti–D and Ni–D PDFs (dashed lines). The restraints were removed during the final stages of the refinements and therefore the restraint criteria are somewhat violated in the resulting configuration.

$g_{ij}(r_j) > L(r_j)$ in the distance range from r_{\min} to r_{\max} , where $L(r_j)$ is a fourth-order polynomial:

$$L(r) = \sum_{n=1}^4 a_n (r - r_0)^n$$

and the r_0 value is set to either r_{\min} (low- r tail) or r_{\max} (high- r tail). A user must specify the $g_{ij}(r_j)$, the side of the peak to be constrained (low- or high- r), the distance interval $[r_{\min}, r_{\max}]$ over which the restraint is applied, the a_n coefficients (obtained by fitting the polynomial to the appropriate part of the $g_{ij}(r)$), and the weight assigned to the penalty term. Fig. B1 illustrates an example of the peak-tail restraints imposed on the metal partial PDFs in ZrTiNiD_2 . The weights of these restraints were reduced to zero during the final stages of the refinements and therefore some violations of the restraint criteria are observed in the final configuration.

References

- [1] Karden E, Ploumen S, Fricke B, Miller T, Snyder K. *J Power Sources* 2007;168(1):2–11.
- [2] Fetsenko MA, Ovshinsky SR, Reichman B, Young K, Fierro C, Koch J, et al. *J Power Sources* 2007;165(2):544–51.
- [3] Berry RL, Raynor GV. *Acta Crystallogr* 1953;6:178–85.
- [4] Shaltiel D, Jacob I, Davidov D. *J Less-Common Met* 1977;53:117–31.
- [5] Yvon K, Fischer P. Hydrogen in intermetallic compounds I. In: Schlapbach L, editor. *Topics in applied physics*, vol. 63. Berlin: Springer; 1988.
- [6] Switendick AC. *Z Phys Chem* 1979;117:89–112.
- [7] Ghoshray K, Bandyopadhyay B, Ghoshtray G, Chatterjee N. *Phys Rev* 1993;B47:8277.
- [8] Sen M, Giri S, Ghoshtray K, Ghoshtray G, Sil S, Chatterjee N. *Phys Rev B* 1996;53:14345.
- [9] Bououdina M, Lambert-Andron B, Ouladdiaf B, Pairis S, Fruchart D. *J Alloys Compd* 2003;356:54–8.
- [10] Sorby MH, Møllergaard A, Delaplane RG, Wannberg A, Hauback BC, Fjellvåg H. *J Alloys Compd* 2004;363:209–16.
- [11] Sorby MH, Møllergaard A, Hauback BC, Fjellvåg H, Delaplane RG. *J Alloys Compd* 2008;457:225–32.
- [12] Nanu DE, Tucker MG, Haije WG, Vente JF, Bottger AJ. *Acta Mater* 2010;58:5502–10.
- [13] Larson AC, von Dreele RB. General structure analysis system, Los Alamos National Laboratory report LAUR; 1994.
- [14] Toby BH. *J Appl Crystallogr* 2001;34:210–3.
- [15] Peterson PF, Gutmann M, Proffen Th, Billinge SJL. *J Appl Crystallogr* 2000;33:1192.
- [16] Keen DA. *J Appl Crystallogr* 2001;34:172–7.
- [17] McGreevy RL, Pusztai L. *Mol Simulat* 1988;1:359–67.
- [18] Tucker MG, Keen DA, Dove MT, Goodwin AL, Hui Q. *J Phys: Condens Matter* 2007;19(33):335218.
- [20] Ravel B, Newville M. *J Synch Radiat* 2005;12:537–41.
- [21] Ice GE, Sparks CJ. *Ann Rev Mater Sci* 1999;29:25–52.
- [22] Daams JL, Villars P, Van Vucht JH. Atlas of crystal structure types for intermetallic phases. Materials Park (OH): ASM International; 1991.
- [23] Jacob I, Stern A, Moran A, Shaltiel D, Davidov D. *J Less-Common Met* 1980;73:369.
- [24] Lengeler B, Zeller R. *J Less-Common Met* 1984;103:337–47.
- [25] Huang RZ, Wang YM, Wang JY, Zhou YC. *Acta Mater* 2004;52:3499–506.